NANO · MICRO small
www.small-journal.com

Rapid and Multimaterial 4D Printing of Shape-Morphing Micromachines for Narrow Micronetworks Traversing

Chen Xin, Dongdong Jin, Rui Li, Dawei Wang, Zhongguo Ren, Bingrui Liu, Chao Chen, Longfu Li, Shunli Liu, Bing Xu, Yachao Zhang, Yanlei Hu, Jiawen Li, Li Zhang, Dong Wu,* and Jiaru Chu*

Micromachines with high environmental adaptability have the potential to deliver targeted drugs in complex biological networks, such as digestive, neural, and vascular networks. However, the low processing efficiency and single processing material of current 4D printing methods often limit the development and application of shape-morphing micromachines (SMMs). Here, two 4D printing strategies are proposed to fabricate SMMs with pH-responsive hydrogels for complex micro-networks traversing. On the one hand, the 3D vortex light single exposure technique can rapidly fabricate a tubular SMM with controllable size and geometry within 0.1 s. On the other hand, the asymmetric multimaterial direct laser writing (DLW) method is used to fabricate SMMs with designable 3D structures composed of hydrogel and platinum nanoparticles (Pt NPs). Based on the presence of ferroferric oxide (Fe_3O_4) and Pt NPs in the SMMs, efficient magnetic, bubble, and hybrid propulsion modes are achieved. Finally, it is demonstrated that the spatial shape conversion capabilities of these SMMs can be used for narrow micronetworks traversing, which will find potential applications in targeted cargo delivery in microcapillaries.

1. Introduction

Untethered micromachines capable of navigating through biological spaces are promising candidates for minimally invasive surgery,[1] imaging-guided delivery,[2] sensing,[3] and targeted therapy applications.[4] Despite tremendous progress in the fabrication, actuation, and functionalization of micromachines, realizing the applications of micromachines in a living body remains challenging.[5] Due to the existence of a large number of intricate networks in living organisms, such as blood vessels, neural networks, and digestive networks (especially for capillaries and venules of ≈5–10[6] and ≈10–30 μm[7]), micromachines with shape-morphing capability possess the promising potential to adapt to these complex micronetworks for a specific application. Based on the small size and controllable shape transformation, shape-morphing micromachines (SMMs) are expected to noninvasively access confined and sensitive regions inside creature bodies, thus revolutionizing diverse biomedical fields.

Recently, a variety of intelligent SMMs that can morph into multiple conformations under various forms of stimuli, including chemical molecules,[8] magnetic fields,[9] and light[10] have been developed. The unique deformability has promoted the widespread applications of SMMs in dynamically tunable micro-optics,[11] targeted delivery,[12] and cargo micromanipulation.[13] Although various micromachines have been integrated with stimulus-responsive characteristics to obtain impressive environmental adaptability, most of them need a multistep 2D manufacturing process to realize the patterning of heterogeneous stimulus-responsive materials.[14] As a high-precision and true 3D processing method, direct laser writing (DLW) and its holographic extension exposure have become a promising candidate for programing various materials[15] and realizing various microstructures,[16–17] such as microscale grippers,[13b] cage-like,[16] tubular,[17] and chiral structures.[18] 4D printed microfish and microgripper have been proposed for precise drug release[5b] and microparticle capture.[13b] However, current DLW-based 4D printing remains problematic. For example, the widely-adopted point-to-point scanning strategy often possesses low efficiency, making it challenging to manufacture SMMs in large quantities rapidly. While for the fabricated SMMs, only single stimulus-responsive material is mainly processed, which may limit the resultant functions of micromachines. Moreover, the controllable navigation of SMMs in narrow and complex micronetworks remains unexplored, which may be an essential step before applying

C. Xin, R. Li, D. Wang, Z. Ren, B. Liu, C. Chen, L. Li, S. Liu, Y. Zhang, Y. Hu, J. Li, D. Wu, J. Chu
Hefei National Laboratory for Physical Sciences at the Microscale
CAS Key Laboratory of Mechanical Behavior and Design of Materials
Department of Precision Machinery and Precision Instrumentation
University of Science and Technology of China
Hefei 230026, China
E-mail: dongwu@ustc.edu.cn

D. Jin, L. Zhang
Department of Mechanical and Automation Engineering
The Chinese University of Hong Kong
Shatin NT, Hong Kong 999077, China
E-mail: lizhang@mae.cuhk.edu.hk

B. Xu
School of Mechanical Engineering
Suzhou University of Science and Technology
Suzhou 215009, China

The ORCID identification number(s) for the author(s) of this article can be found under https://doi.org/10.1002/smll.202202272.

DOI: 10.1002/smll.202202272

SMMs in dynamic physiological environments in vivo. Thus, combining stimulus-responsive hydrogels with the 4D printing technique to develop SMMs is expected to be a practical approach for further biomedical studies, especially in traversing biomimetic microscale networks by active deformation for cargo delivery.

Here, we propose two selectable strategies to process SMMs for traversing micronetworks smaller than themselves. First, to solve the limitation of low processing efficiency, one-step vortex exposure is capable of fabricating trumpet-shaped micromachines (TSMMs) with a large quantity (>5000) in only 10 min. Based on spatial light modulation technology, a focused laser beam with a gaussian intensity distribution is modulated into a gradient 3D beam with a trumpet-like distribution for rapid construction of TSMMs in one-step exposure (Movie S1, Supporting Information). In addition, to extend the types of printing materials and then realize more functions, asymmetric multimaterial DLW is used to directly print complex 3D microfish with stimulus-responsive hydrogel and catalyst platinum nanoparticles (Pt NPs), which integrates designable shape morphing and bubble-propelling capabilities. Eventually, both SMMs can achieve controllable traverse through the networks narrower than themselves via shape conversion. We believe that SMMs prepared by these two methods will find promising applications in targeted cargo delivery in complex biological micronetworks.

2. Results and Discussion

The experimental setup is implemented for shape-morphing TSMM fabrication, as illustrated in **Figure 1**a. The vortex structural beam is modulated by loading vortex holography (VH) on a spatial light modulator (SLM). By controlling the size of the optical vortex entering the pupil, the trumpet-shaped 3D vortex beam is generated by optical focusing through a high numerical aperture objective lens. Thus, a TSMM can be fabricated through a single exposure instead of point-to-point scanning.

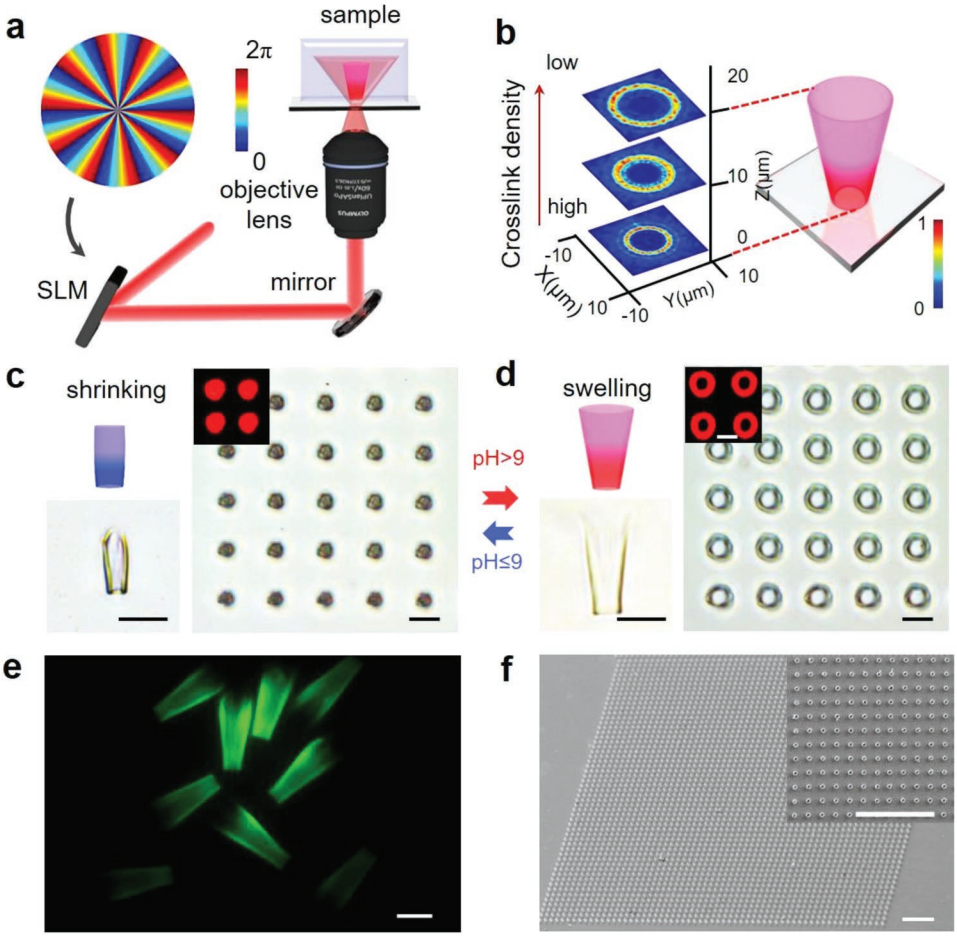

Figure 1. Shape-morphing TSMMs fabricated by one-step gradient optical vortices exposure. a) SLM-based optical setup for TSMM manufacturing. An SLM displays a designed vortex beam hologram to modulate femtosecond laser into a trumpet-shaped structured beam. The manufacturing time of each TSMM is 100 ms. b) The simulated light intensity distribution of the 3D optical vortex in different z-planes under the oil immersion objective lens. As the distance from the focus center is farther, the diameter of the light field is larger, and the intensity is weaker. The shrinkage c) and expansion d) of the TSMMs array in solutions of different pH values have a good consistency. e) The green fluorescence microscope image of TSMMs clearly shows the hollow body of the structure. f) Based on high-efficiency 3D optical vortex exposure processing, 5000 TSMMs can be fabricated within 10 min. Scale bar: c–e) 25 μm, f) 200 μm.

The phase of the vortex beam loaded on the SLM can be presented as

$$\mathrm{Phase}(x,y) = \mathrm{mod}(l\varphi + \frac{2\pi x}{\Delta}, 2\pi) \quad (1)$$

Where Phase(x,y) represents the phase distribution in Cartesian coordinate, φ = arctan(y/x), topological charge l determines the local radius of maximum intensity at angle φ and blazed grating period Δ = 15 μm. Furthermore, to provide deeper insights into the geometry of TSMMs, the Debye vectorial diffraction theory is adopted to simulate the focused vortex beams. The intensity distribution in the focal region can be rewritten as

$$\boldsymbol{E}(x,y,z) = -\frac{iC}{\lambda}\int_0^{\alpha}\int_0^{2\pi} \sin\theta E_{\mathrm{obj}}(\theta,\varphi)\sqrt{\cos\theta}\,\boldsymbol{P}(\theta,\varphi) \times \exp[ikn(x\sin\theta\cos\varphi + y\sin\theta\sin\varphi + z\cos\theta]d\theta d\varphi \quad (2)$$

Where C is a constant, $E_{\mathrm{obj}}(\theta,\varphi)$ is the electric field at the entrance pupil of the objective, $k = 2\pi/\lambda$ is the wave number, and the wavelength of incident light is 800 nm. n is the refractive index of the immersion medium, θ represents the focusing angle of the objective lens, and φ is the azimuthal angle of the object plane. α is the maximum focusing angle of the objective lens and can be expressed by the formula α = arc cos (NA/n). $\boldsymbol{P}(\theta, \varphi)$ indicates the polarization state of the EM field in the focal region, which can be rewritten as

$$\boldsymbol{P}(\theta,\varphi) = [1 + (\cos\theta - 1)\cos^2\varphi]\boldsymbol{i} + [(\cos\theta - 1)\cos\varphi\sin\varphi]\boldsymbol{j} - (\sin\theta\cos\varphi)\boldsymbol{k} \quad (3)$$

for incidence with linear polarization at X direction, as used in our experiment.

According to the simulation, all trumpet-shaped vortex beams have different beam intensities in different planes of the propagation direction. As the distance between the beam plane and the focus center increases, the electric density of the beam gradually decreases (Figure 1b). In this way, under a single exposure, the ring structure of the TSMM has different thicknesses at different heights, resulting in different degrees of morphing. In our study, the TSMMs are printed in a hydrogel mainly contained with acrylic acid (Figure S1, Supporting Information). The corresponding morphing mechanism is that the carboxyl groups are protonated at a low pH value (pH < 9), and the network collapses, causing the shrinkage of the hydrogel.[19] As illustrated in Figure 1c, the TSMMs shrink in a solution environment with a pH < 9 (Movie S2, Supporting Information). On the contrary, TSMMs swell in a solution environment with a pH > 9 (Figure 1d), in which the carboxyl groups are deprotonated and negatively charged, generating electrostatic repulsion forces between the molecular chains, resulting in a significant expansion of the hydrogel network. Furthermore, the reversible morphing test of the TSMM array proves that their morphing has a good consistency. Figure 1e shows that the TSMM is separated from the substrate and dispersed in NaOH, with a typical height of 60 μm and a minimum center diameter of 10 μm. Since our method can develop a TSMM within 100 ms exposure, thousands of TSMMs (>5000) can be manufactured within a few minutes. Figure 1f is a 45° tilted SEM image of the polymerized TSMMs on a glass substrate, and the image inserted in the upper left corner is a top view SEM image. Therefore, this processing method can reliably and efficiently manufacture shape-morphing TSMM arrays with controllable shapes, which opens up potential application prospects for dynamic optical switches and microcargo traps.

An important advantage of the one-step optical vortices exposure manufacturing is the flexibility to control the geometry of the 3D TSMM. First, the topological charges of VHs could significantly affect the diameter and length of TSMM (**Figure 2**a). By optical simulation and experimental measurement (Figure 2b), it is found that the shapes of vortex beams with different topological charges are all trumpet-shaped in 3D space. Subsequently, deformation tests are performed on TSMMs with different parameters, which shows that TSMMs of different sizes swell in a solution with pH > 9 (Figure 2c), and contract in a solution with pH < 9 (Figure 2d). In Figure 2e, when the topological charge increases from 2 to 30, the focal plane diameter of the optical vortex increases from 4 to 22 μm, where the experimental values have strong consistency with the simulation (Figures S2 and S3, Supporting Information). We extract the cross-sectional beam intensity at different positions along the optical axis. It is found that the farther from the center of the focal plane, the weaker the beam intensity. Among them, when the topological charge is 10, the beam intensity at 30 μm away from the center of the focal plane is only a quarter of the center of the focal plane (Figure 2f). The head of the TSMM corresponds to the center of the vortex beam with a higher energy density, and the tail corresponds to the far end of the vortex beam with a lower energy density than the head. TSMM has a low degree of cross-linking and a high degree of cross-linking in the tail and head, leading to a much larger shrinkage ratio of the tail than the head. Thereby, in the shrinking state, the diameter of the TSMM tail is smaller than that of the head (Figure 2g). For a TSMM exposed to an optical vortex with a topological charge of 10, when it shrinks, the diameter of the tail shrinks from 20 to 2 μm, which is smaller than the diameter of the head ≈5 μm (Figure 2g). In addition to the parameters of the optical vortices, the single exposure time and power also affect the geometry of the TSMM. By adjusting the exposure time (≈100–500 ms) and power (≈40–80 mW), shape-morphing TSMMs with a height ranging from 10 to 50 μm can be easily manufactured in a contracted state. Correspondingly, as the height increases, the center diameter of TSMMs increases from about 4 to 10 μm. It is worth noting that when the exposure time is too long, multiple soft flagella will grow on the tail of TSMM due to the stray light spots involved in the exposure (Figure S4, Supporting Information). TSMMs with flagella on the tail shrinks tighter, causing the flagella to become entangled together. On the contrary, when the pH of the solution is >9, both the diameter and length of TSMMs increase, reaching the maximum of 40 and 90 μm, respectively (Figure S4, Supporting Information). Briefly, benefiting from the flexible adjustment of the optical vortices and exposure processing parameters, smart micromachines of various sizes can be rapidly processed.

To make our TSMMs have magnetic drive performance, they are incubated with the magnetic nanoparticle suspension for

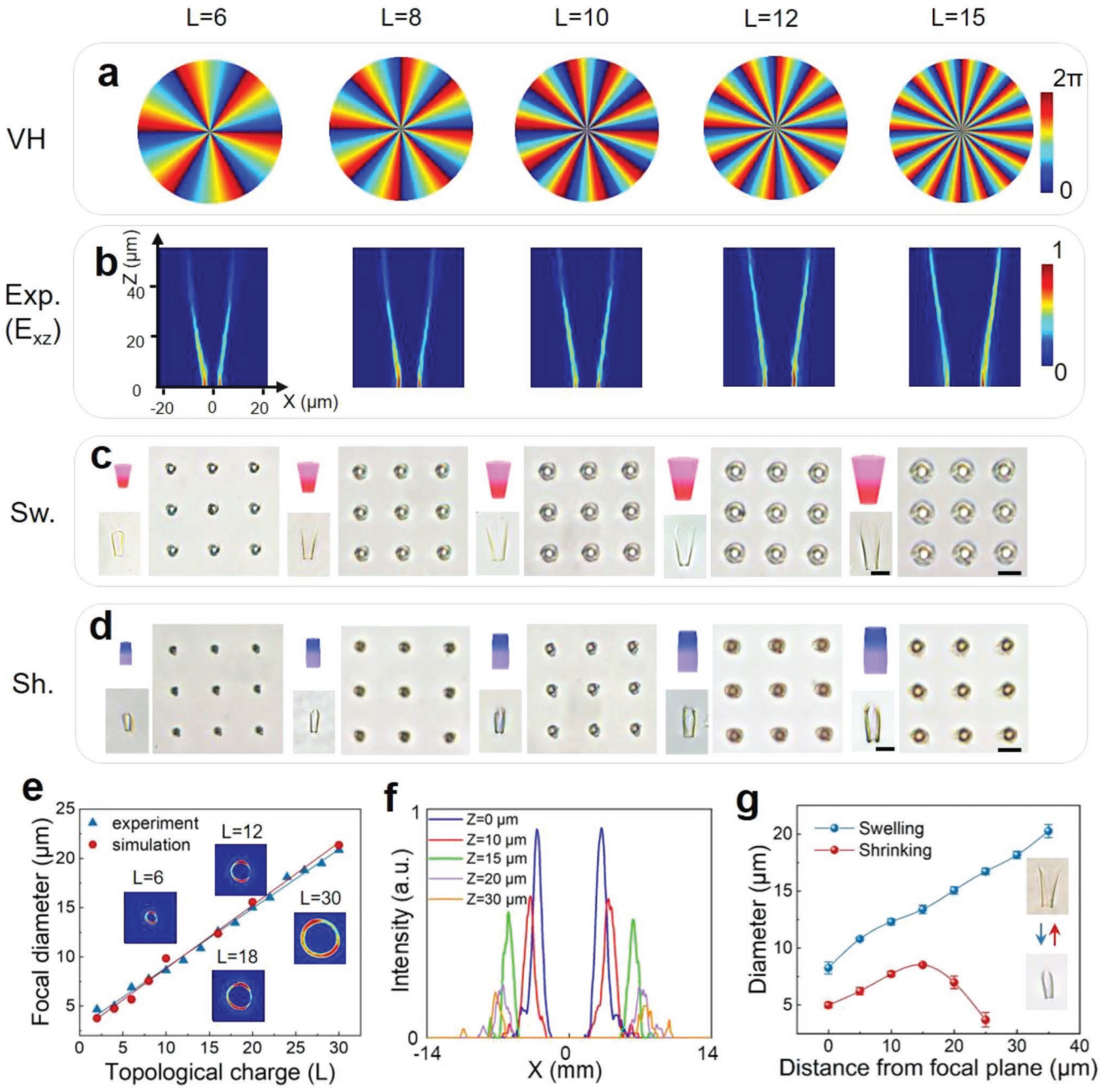

Figure 2. Flexible control of shape-morphing TSMM with various topological charges of optical vortices. a) A series of VHs with different topological charges (L = 6, 8, 10, 12, 15). b) The experimental optical field of the different VHs under high NA objective lens in x–z plane. The TSMMs produced by these modulated vortex beams are expanded c) at pH > 9 and in a contracted state d) at pH < 9. e) Measured and calculated focal diameter of the optical vortex as a function of topological charge. f) The vertical intensity distribution of the simulated light field at different positions (0–30 μm) far away from the focus center. g) During expansion and contraction, the diameter of TSMM at different positions from the focal center. Scale bars: b–d) 20 μm. All the error bars represent the standard deviation ($n = 3$).

12 h to make the surface uniformly adhere to a layer of ferro-ferri oxide (Fe_3O_4) NPs (Figure S5a, Supporting Information). After being covered by a layer of Fe_3O_4 NPs, the TSMM turned from transparent to brown-black under the optical microscope. According to scanning electron microscope (SEM) measurement, the diameter of magnetic nanoparticles is ≈200 nm (Figure S6, Supporting Information). Figure S7 (Supporting Information) shows that the adhesion of Fe_3O_4 NPs has no negative effect on the morphing characteristics of TSMM. Subsequently, the TSMMs is peeled from the substrate by a microneedle system.[4c] In this way, they can be flexibly operated by the external magnetic field (electromagnetic coils, 15 Hz 2 mT, or a permanent magnet, ≈10 mT, Figures S8 and S9, Movie S3, Supporting Information). Here, a permanent magnet is chosen to propel the TSMM because of its simplicity, convenience, and strong magnetic field, which showed great

potential in clinical trials.[20] Therefore, by combining wireless magnetic motion control and shape conversion capabilities, TSMM can carry out dynamic transportation of various microcargos. Here, TSMM is used to manipulate silica microspheres via shape transformation, including selection, active grasping, transport, and release (Figure S5c, Supporting Information). It can be observed that the TSMM loaded with microspheres can be flexibly guided in the microliquid environment to complete the tracking of the patterned trajectory of the "MNE." Finally, the release of the microspheres is achieved under an ultrasonic field. Figure S5d (Supporting Information) shows that the TSMMs gradually crack with time under the ultrasonic field (500 W, 50 s).

In addition to open spaces, microrobots often need to perform tasks in complex networks. However, most of the previous micromachines cannot pass through some capillaries (≈8–10 μm)[6] and venules (≈10–30 μm)[7] smaller than their size due to their inability to change their shape. Here, as a representative, a larger size TSMM is selected to traverse a micronetwork (30 μm) comparable to the venule size. In this work, we prepared various microfluidic channels whose width is smaller than the initial body width of TSMM (30 μm channel diameter) so that TSMM cannot pass through the channel in the expanded state. **Figure 3**a is a conceptual diagram showing TSMM passing through narrow microchannels. Specifically, when the solution pH is >9, the tail end of the TSMM is stuck in the middle of the hourglass-shaped microchannel. At this time, by adjusting the pH of the solution to <9, the TSMM can pass through the narrow channel after shrinking (Figure 3b; and Movie S4, Supporting Information). Similarly, the TSMM can traverse microfences, straight, and curved channels through shape switching (Figure 3c–e; and Movies S5 and S6, Supporting Information). Furthermore, through flexible adjustment of the direction of the magnetic field, there is no difficulty for TSMM to traverse more complicated microchannels in the shape of Arabic numerals, such as ′0, 2, 9″ (Figure 3f). Compared with the past tubular micromotors, TSMM can adjust the size to pass through narrow microchannels, which further increases the environmental adaptability of the micromachines.

In addition to efficiently fabricating micromachines, expanding the types of functional materials manufactured by 4D printing is also meaningful for developing multifunctional micromachines. Therefore, we propose the use of asymmetric multimaterial direct laser writing technology to process SMMs composed of hydrogel and metal nanoparticles. For example, we designed a shape-morphing microfish (SMMF), whose fins and tails are fabricated by asymmetric laser direct writing density scanning, resulting in anisotropic expansion rates for controllable deformation. Asymmetric DLW is achieved by asymmetric scanning point spacing, as shown in the schematic diagram in **Figure 4**a. Both the fin and tail of fish contain asymmetric scanning point spacing distributions of 500 nm (pink) and 200 nm (red), respectively. Compared with a scanning point spacing of 500 nm, a scanning point spacing of 200 nm corresponds to a higher hydrogel crosslink density. The low crosslink part of the hydrogel will have a larger shrinkage than the high crosslink part, so the integration of two crosslink degrees in the hydrogel structure can produce asymmetric shape morphing. Generally, it takes 8 min to fabricate an SMMF with a size of 41 × 58 μm and a surface roughness of 18.92 nm (Figure S10, Supporting Information). At different pH values, SMMF exhibits different shape-morphing times, ranging from 0.5 s at pH = 1 to 10 s at pH = 5 (Figure S11, Supporting Information). Experiments show these SMMFs have stable deformation under 50 cycles of contraction and expansion. (Figure S12, Supporting Information). In addition to hydrogel with designable morphing, metal nanoparticles can be integrated into hydrogel by the same laser microfabrication system, as shown in Figure 4a,b; and Movie S7 (Supporting Information). Here, Pt is chosen as a representative because it is the common source material for bubble-propelled micromachines, achieved by Pt-catalyzed hydrogen peroxide splitting jet bubbles. Compared with the aforementioned magnetic driving, the bubbles actuation mode has been widely investigated due to its low power consumption, convenient operation, and no need for external driving equipment.[21] Elemental analysis shows that SMMF contains carbon (C), oxygen (O), and platinum (Pt), which only exists in the middle of the fishtail and are responsible for bubbles generation (Figure 4c). When the SMMF is immersed in 10 wt% hydrogen peroxide solution, it can be powered by the bubbles produced from the tail. As shown in Figure 4d–g, SMMFs show diverse swimming characteristics in different pH value environments, where the orange and blue images represent sodium hydroxide (pH > 9) and deionized water (pH <9) with hydrogen peroxide solution, respectively. It is worth mentioning that the diameters of the bubbles excluding from fishtail in high pH values are bigger than that in low pH values due to fishtail morphing, which explains the SMMFs showing different swimming speeds (pH >9, ≈48 μm s^{-1} and pH < 9, ≈18.9 μm s^{-1}) and trajectories in different solvents (Movie S8, Supporting Information). Another reason is that the swelling SMMFs have different adhesion to glass substrate compared with the contractive SMMFs. The bubble's diameters are quantitatively investigated in Figure 4h, where the bubble's diameters are about 3.62 μm in deionized water and 5.79 μm in a sodium hydroxide (Movie S9, Supporting Information). In addition, the tail increases from 18.7 to 29.1 μm, and the fin's width increases from 28.1 to 40.7 μm as well (Figure 4i). All in all, a multimaterial SMMF with shape switching and bubble-propelling capabilities has been fabricated. In particular, SMMF can also change shape from pH ≈ 7.4 (PBS) to pH <7 due to partial hydrogen bond disruption in phosphate sustained-release solution, which provides feasibility for in vivo applications (Figure S13, Supporting Information). Besides, the processed Pt is still unfriendly to the biological environment, and bio-friendly materials will be expanded in the future.

Natural creatures often need some distinct strategies to deal with changeable living environments, where the most common method is shape morphing. Thus, a hybrid bubble-magnetic actuated SMMF is demonstrated to adapt to the surrounding environment and successfully pass through a complex maze by fins morphing (**Figure 5**a). Here, the bubbles are used for rapidly driving the SMMF, while the weak magnetic field is used for remotely controlling the movement direction. In this way, we can combine the advantages of both driving methods and avoid their disadvantages. Precise direction control of SMMF is impossible for bubbles actuation, while it is also too difficult to set up a strong magnetic field for actuating the SMMF from

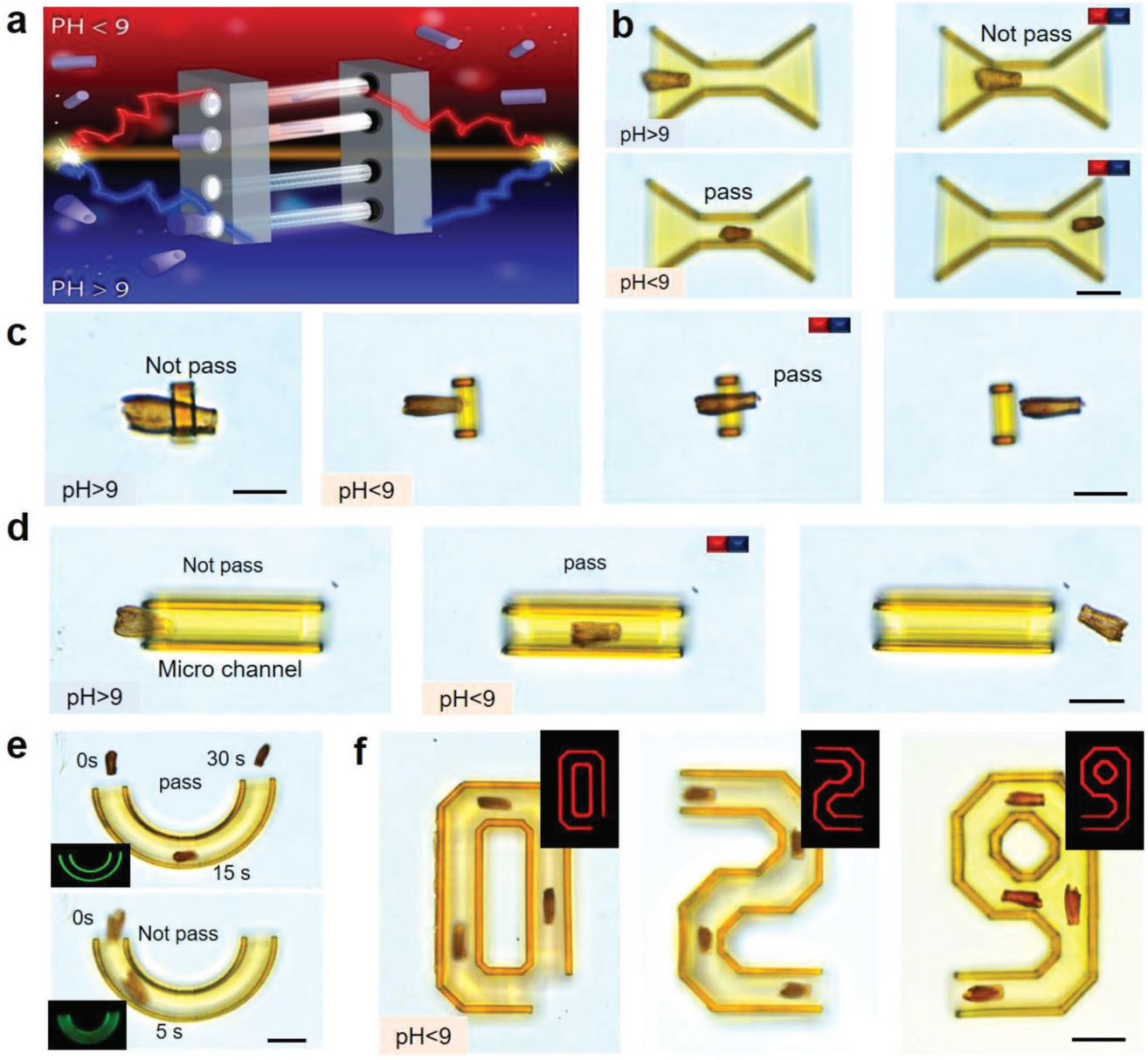

Figure 3. Magnetic TSMM passes through narrow channels by shape switching. a) A schematic diagram of TSMM traversing a microchannel smaller than its size. b) Time-lapse images of magnetic TSMM passing through an hourglass-shaped microchannel. c) Magnetic TSMM passes through a gate, straight channel d), and curved channel e) by shape transformation. f) Magnetic TSMM traverses designable microchannels, including several channels in the shape of Arabic numbers "0, 2, 9". Scale bar: b–e) 50 μ.

a remote distance. At first, we utilize ultraviolet (UV) lithography to fabricate a complex maze pattern for SMMF cruising (Figure 5b). In particular, to highlight the environmental adaptability of SMMF, we fabricate a 35 μm width microgap in the center of the maze according to the analysis of SMMF morphing capability in early study. By combining shape morphing with hybrid bubble-magnetic propelling, the SMMF can pass through the complex maze with a 35 μm microgap by fins shrinking (Figure 5e), which is narrower than SMMF with fully extended fins (Figure 5c). As shown in Figure 5d, the width of the SMMF (41 μm) with opened fins is bigger than 35 μm, so it is stuck in the gap. Inversely, the fins of SMMF suddenly shrink less than 35 μm when we adjust the pH value to lower than 9 (Figure 5f). At last, the full trajectory of SMMF cruising the micromaze is finished in 90 s (Figure 5i), where the start and finish points are marked by blue and red pentagrams (Movie S10, Supporting Information). It is also observed that the SMMF is in swelling and shrinking state at the start and finish point in the enlarged image, respectively (Figure 5g,h). Although in vitro micronetworks traversal of SMMF has been achieved, the current solution is indeed challenging in practical applications, and future efforts will be made to develop some responsive (magnetic, optical) deformable devices that are more suitable for in vivo applications.

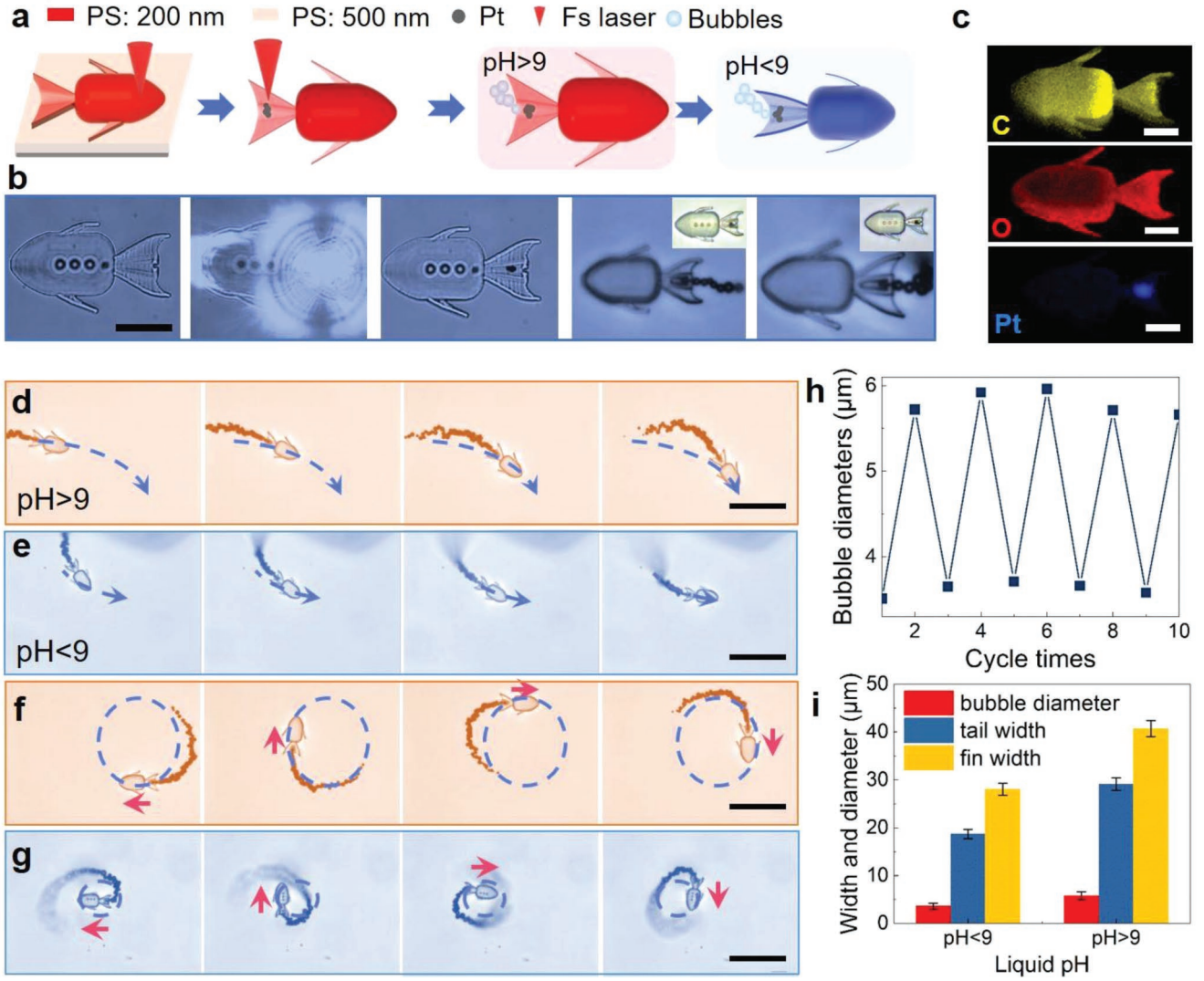

Figure 4. Bubble-propelled SMMF adjusting swimming speed by tail morphing. a,b) Schematic illustration of the processing method and the optical images of the SMMF deposited with platinum (Pt) in its tail, respectively (Movie S7, Supporting Information). c) The elemental analysis of the SMMF by EDS, which verifies the existence of the Pt. d,f) The swelling SMMF steered along the arc and circle track in solution (pH > 9), respectively. e,g) The contractive SMMF steered along the arc and circle track in solution (pH < 9), respectively (Movie S8, Supporting Information). h) The repetition test of bubbles diameters with the change of pH value. i) The produced bubbles diameters, tail, and fins widths of the SMMF in solution with high and low pH values, respectively. All standard deviations are obtained from three parallel tests ($n = 3$). Scale bars, b) 20 μm, c) 10 μm, d–g) 100 μm.

3. Conclusion

In summary, we propose two processing methods for fabricating SMMs to traverse narrow micronetworks. One approach uses 3D optical vortices to process TSMMs in one-step within 100 ms. This method is simple and efficient and can manufacture SMMs in large quantities. Another method uses asymmetric multimaterials laser direct writing processing technology to fabricate SMMF with shape-morphing and bubble-propulsion capabilities. This method is suitable for processing multi-materials, complex, and specific three-dimensional structures. Both TSMM and SMMF can be driven at high speed by magnetic fields and bubbles. Finally, traverse narrow channels smaller than their size through shape switching. It is worth noting that the two processing strategies and the three propulsion modes each have their advantages, and we provide these alternatives to match the most suitable application scenarios. In the future, we believe these SMMs can be modified to handle a variety of cargoes, including therapeutic agents and diagnostic sensors, which will become widely used tools in complex micronetworks in biomedicine.

4. Experimental Section

Preparation of pH-Responsive Hydrogel: First, 1.6 g N-isopropylacrylamide (NIPAAm, 98%), 0.8 mL Acrylic acid (AAc, 99%), and 0.15 g polyvinylpyrrolidone (PVP, average M_w ≈1, 300 000) are added to 1 mL ethyl lactate (EL, 98%) and then stirred vigorously.

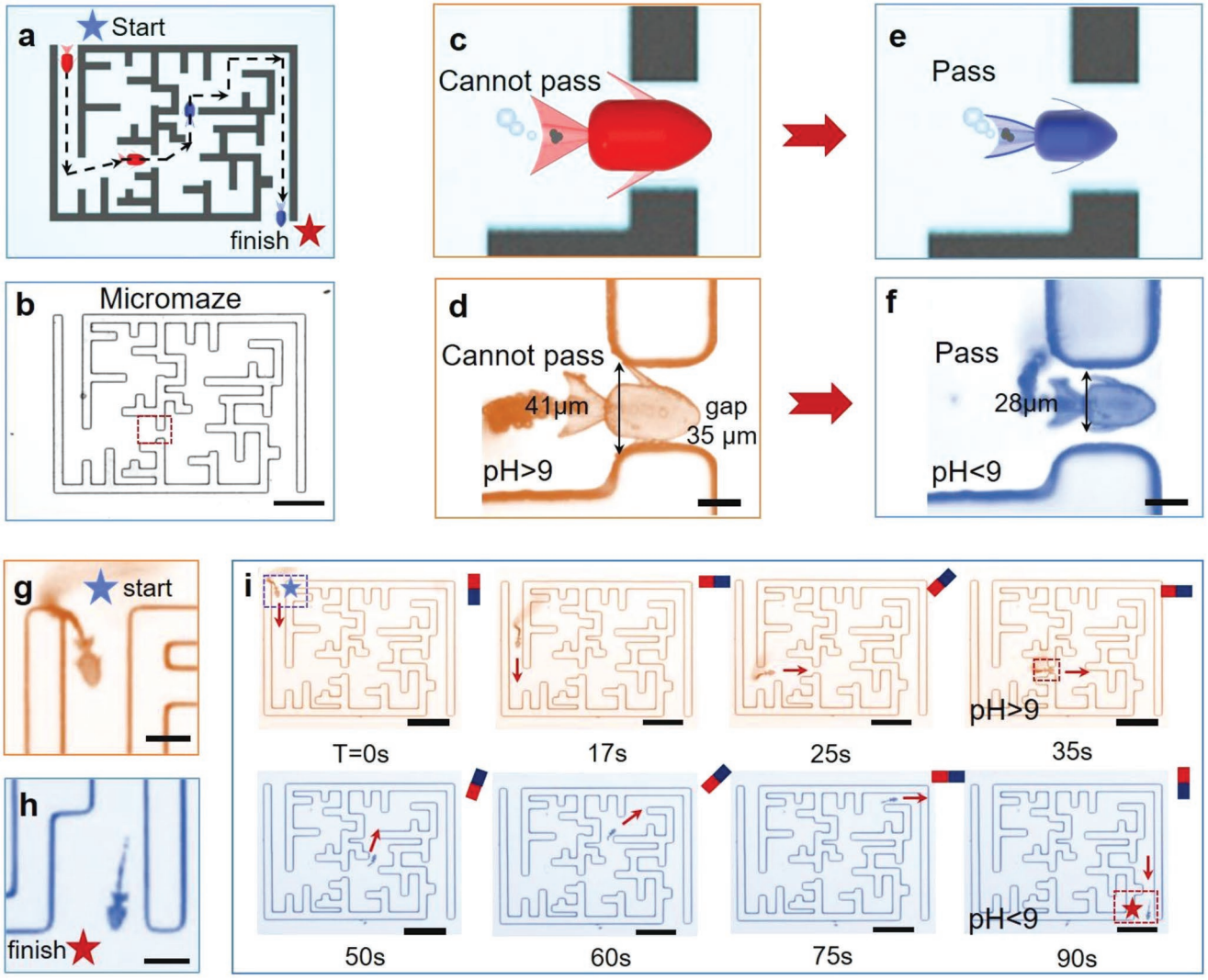

Figure 5. Hybrid bubble-magnetic actuated SMMF passing through the complex maze by fins morphing. a) The schematic illustration of the SMMF swimming across the maze. b) The optical image of the micromaze is fabricated by UV lithography. c,d) The schematic illustration and optical images of SMMF with opened fins (41 μm width) cannot pass through the microgap with 35 μm width. e,f) The schematic illustration and optical images of SMMF with closed fins (29 μm width) can pass through the microgap to arrive at the finish point of the maze. The swelling g) and shrinking h) SMMF at the start and finish point of micromaze, respectively. i) The time-lapse images of SMMF swimming across the micromaze actuated by bubbles and magnetic field (Movie S10, Supporting Information). Scale bars, e,f) 20 μm, g,h) 50 μm, d,i) 200 μm.

Then, 2.5 mL of the above solution, 0.5 mL dipentaerythritol hexaacrylate (DPEHA,98%), 0.5 mL triethanolamine (TEA, 99%), and 100 μL 4,4-bis(diethylamino) benzophenone (EMK, 97%)/*N*, *N*-dimethylformamide (DMF, 99.5%) solution (20 wt%) are mixed, followed by stirring 12 h, to mix each component completely. Finally, the precursor is kept in yellow light condition to avoid unnecessary light exposure. In our hydrogel, the TEA and EMK is photosensitizer and photoinitiator, respectively. Both AAc and NIPAAm are monomers to form a hydrogel network. Meanwhile, the crosslinker DPEPA is used to support the poly (AAc-*co*-NIPAAm) hydrogel framework. PVP is an additive to enhance the support by increasing the solution viscosity, facilitating the construction of freestanding 3D architectures.

Design and Fabrication of Magnetic TSMMs: A typical femtosecond laser writing system source is a mode-locked Ti: sapphire laser oscillator (Chameleon Vision-S, Coherent Corp, central wavelength: 800 nm, repetition rate: 80 MHz, pulse width: 75 fs). First, the processing is performed using femtosecond laser direct writing technology. The polymer molecular chains at the laser focus are polymerized. The processed sample is immersed in a developing solution (ethanol or isopropyl alcohol) for 15 min to remove the uncured hydrogel. The developed sample is then taken out and placed under an inverted microscope for in situ observation. To avoid the fast evaporation of ethanol, pure water is dripped around the sample. When the NaOH solution is dropped, the sample swells, and then dilute hydrochloric acid is added dropwise to make the sample shrink. To maintain the pH of the solution, all shape morphing of the SMMs are tested at room temperature (25 °C).

Design and Fabrication of Magnetic SMMF: At first, the SMMF is fabricated by direct laser writing with 20 mW exposure power. To prevent the micromachine from making large-area contact with the substrate, several micropillar structures with a diameter of 2 μm at the bottom of the micromachine were added. A 1:1 volume precursor solution was mixed comprised of 0.7 M of the $(NH_4)_2[PtCl_4]$ and 1.0 M of the iron (III) oxalate, and Pt was reduced using the above mode-locked titanium: sapphire laser centered at 800 nm. The movement of the sample is completed by a nano-positioning stage (E545, from Physik

Instrumente GmbH & Co. KG, Germany) with nanometer resolution and a 200 × 200× 200 μm^3 moving range to precisely locate microstructures. Thus, the platinum (Pt) is accurately deposited in the fishtail to generate bubbles for effective actuation, where the error of reduction position is less than 0.5 µm. To get the bubble-propelled SMMF, an aqueous H_2O_2 solution with a 10 wt% concentration is used as chemical fuel.

Remote Magnetic Motion Control of SMMs: The samples are immersed in the magnetic particles (Fe_3O_4 NPs) suspension cultured for 12 h to absorb nanoparticles. Here, the surface of Fe_3O_4 NPs (≈200 nm) has been wrapped in a layer of silica (SiO_2) to prevent them from reacting with acids (pH = 1 and 4) (Figures S8 S14, Supporting Information). Subsequently, a homemade 3D mobile platform and capillary microneedle was used to peel off the SMM and it was transferred with a microliter pipette. At last, the magnetic actuation of SMMs is realized by a permanent magnet (diameter and height 5 mm, N52, NdFeB) (Figure S9). We use a microliter pipette to add hydrochloric acid (pH ≈1) and NaOH (pH ≈12) to the edge of the sample, which changes the pH of the entire sample through the diffusion of the liquid.

Characterization: Optical micrographs are taken with an inverted fluorescence microscope (Leica DMI3000b). The SEM images are collected with a secondary electron SEM (ZEISS EVO18) operated at an accelerating voltage of 10 keV after depositing ≈10 nm gold.

Statistical Analysis: All data were expressed as mean ± standard deviation (SD), with $n = 3$ per group.

Supporting Information

Supporting Information is available from the Wiley Online Library or from the author.

Acknowledgements

This work was supported by the National Natural Science Foundation of China (Nos. 61927814, 52122511, 51875544, and 91963127), Major Scientific and Technological Projects in Anhui Province (No. 201903a05020005), the Fundamental Research Funds for the Central Universities (No. WK2090000024), the China Postdoctoral Science Foundation (No. 2021M703120), and the Open Project Program of Wuhan National Laboratory for Optoelectronics (No. 2019WNL0KF014), Open Research Fund of Advanced Laser Technology Laboratory of Anhui Province (No. AHL2020KF01). L.Z. thanks to the financial support from the Hong Kong Research Grants Council (RGC) with project No. JLFS/E-402/18, CAS-Croucher Funding Scheme for Joint Laboratories with Project No. CAS20403, the ITF project with Project No. MRP/036/18X is funded by the HKSAR Innovation and Technology Commission (ITC), and the support from Multiscale Medical Robotics Center (MRC), InnoHK, at the Hong Kong Science Park. The authors acknowledge the Experimental Center of Engineering and Material Sciences at USTC for the fabrication and measuring of samples. This work was partly carried out at the USTC Center for Micro and Nanoscale Research and Fabrication.

Conflict of Interest

The authors declare no conflict of interest.

Author Contributions

C.X. and D.-D.J. contributed equally to this work. C.X., D.W., and L.Z. conceived the idea and designed the project. C.X., D.-D.J., D.-W.W., Z.-G. R., R.L., and B.-R.L. performed all the experiments and the characterization. C.X., D.-D.J., C.C., and L.-F.L. completed data analysis and figure depicture. R.L., B.X., and S.-L.L. helped with setting up the printing system. Y.-L.H. and J.-W.L. helped with the artificial network fabrication. C.X., D.W., and L.Z. wrote and revised the paper. D.W., L.Z., and J.-R.C. supervised the project.

Data Availability Statement

The data that support the findings of this study are available in the supplementary material of this article.

Keywords

4D printing, micromachines, micronetwork traversing, responsive hydrogels, shape morphing

Received: April 11, 2022
Revised: July 12, 2022
Published online:

[1] a) Y. Dong, L. Wang, V. Iacovacci, X. Wang, L. Zhang, B. J. Nelson, *Matter* **2022**, *5*, 77; b) W. Gao, R. Dong, S. Thamphiwatana, J. Li, W. Gao, L. Zhang, J. Wang, *ACS Nano* **2015**, *9*, 117.

[2] a) Q. Wang, L. Zhang, *ACS Nano* **2021**, *15*, 149; b) Q. Wang, K. F. Chan, K. Schweizer, X. Du, D. Jin, S. C. H. Yu, B. J. Nelson, L. Zhang, *Sci. Adv.* **2021**, *7*, eabe5914.

[3] a) B. E.-F. de Ávila, P. Angsantikul, D. E. Ramírez-Herrera, F. Soto, H. Teymourian, D. Dehaini, Y. Chen, L. Zhang, J. Wang, *Sci. Robot.* **2018**, *3*, eaat0485; b) W. Zhu, J. Li, Y. J. Leong, I. Rozen, X. Qu, R. Dong, Z. Wu, W. Gao, P. H. Chung, J. Wang, S. Chen, *Adv. Mater.* **2015**, *27*, 4411; c) M. Pacheco, B. Jurado-Sanchez, A. Escarpa, *Anal. Chem.* **2018**, *90*, 2912.

[4] a) B. Wang, K. Kostarelos, B. J. Nelson, L. Zhang, *Adv. Mater.* **2020**, *4*, 2002047; b) S. Tottori, L. Zhang, F. Qiu, K. K. Krawczyk, A. Franco-Obregon, B. J. Nelson, *Adv. Mater.* **2012**, *24*, 811; c) C. Xin, L. Yang, J. Li, Y. Hu, D. Qian, S. Fan, K. Hu, Z. Cai, H. Wu, D. Wang, *Adv. Mater.* **2019**, *31*, 1808226; d) U. Bozuyuk, O. Yasa, I. C. Yasa, H. Ceylan, S. Kizilel, M. Sitti, *ACS Nano* **2018**, *12*, 9617.

[5] a) J. Li, B. E.-F. de Ávila, W. Gao, L. Zhang, J. Wang, *Sci. Robot.* **2017**, *2*, eaam6431; b) C. Xin, D. Jin, Y. Hu, L. Yang, R. Li, L. Wang, Z. Ren, D. Wang, S. Ji, K. Hu, D. Pan, H. Wu, W. Zhu, Z. Shen, Y. Wang, J. Li, L. Zhang, D. Wu, J. Chu, *ACS Nano* **2021**, *15*, 18048.

[6] A. Lee, A. Hudson, D. Shiwarski, J. Tashman, T. Hinton, S. Yerneni, J. Bliley, P. Campbell, A. Feinberg, *Science* **2019**, *365*, 482.

[7] a) K. Kucharz, K. Kristensen, K. B. Johnsen, M. A. Lund, M. Lønstrup, T. Moos, T. L. Andresen, M. J. Lauritzen, *Nat. Commun.* **2021**, *12*, 4121; b) H. H. Lipowsky, L. Gao, A. Lescanic, *Am. J. Physiol. Heart Circ. Physiol.* **2011**, *301*, H2235.

[8] a) Y.-L. Zhang, Y. Tian, H. Wang, Z.-C. Ma, D.-D. Han, L.-G. Niu, Q.-D. Chen, H.-B. Sun, *ACS Nano* **2019**, *13*, 4041; b) Y. Hu, Z. Wang, D. Jin, C. Zhang, R. Sun, Z. Li, K. Hu, J. Ni, Z. Cai, D. Pan, *Adv. Funct. Mater.* **2020**, *30*, 1907377; c) A. Cangialosi, C. Yoon, J. Liu, Q. Huang, J. Guo, T. D. Nguyen, D. H. Gracias, R. Schulman, *Science* **2017**, *357*, 1126.

[9] a) J. Cui, T.-Y. Huang, Z. Luo, P. Testa, H. Gu, X.-Z. Chen, B. J. Nelson, L. J. Heyderman, *Nature* **2019**, *575*, 164; b) Y. Kim, H. Yuk, R. Zhao, S. A. Chester, X. Zhao, *Nature* **2018**, *558*, 274.

[10] a) A. Mourran, H. Zhang, R. Vinokur, M. Möller, *Adv. Mater.* **2017**, *29*, 1604825; b) O. M. Wani, H. Zeng, A. Priimagi, *Nat. Commun.* **2017**, *8*, 15546; c) B. Han, Y. L. Zhang, L. Zhu, Y. Li, Z. C. Ma, Y. Q. Liu, X. L. Zhang, X. W. Cao, Q. D. Chen, C. W. Qiu, *Adv. Mater.* **2019**, *31*, 1806386.

[11] a) Z. C. Ma, X. Y. Hu, Y. L. Zhang, X. Q. Liu, Z. S. Hou, L. G. Niu, L. Zhu, B. Han, Q. D. Chen, H. B. Sun, *Adv. Funct. Mater.* **2019**, *29*, 1903340; b) L. Zhu, Y.-L. Zhang, H.-B. Sun, *Light: Adv. Manuf.* **2021**, *2*, 84.

[12] a) J. Tu, W. Gao, *Sci. Robot.* **2020**, *5*, eabf1390; b) Z. Zheng, H. Wang, L. Dong, Q. Shi, J. Li, T. Sun, Q. Huang, T. Fukuda, *Nat. Commun.* **2021**, *12*, 411; c) C. Li, G. C. Lau, H. Yuan, A. Aggarwal, V. L. Dominguez, S. Liu, H. Sai, L. C. Palmer, N. A. Sather, T. J. Pearson, *Sci. Robot.* **2020**, *5*, eabb9822.

[13] a) Z.-C. Ma, Y.-L. Zhang, B. Han, X.-Y. Hu, C.-H. Li, Q.-D. Chen, H.-B. Sun, *Nat. Commun.* **2020**, *11*, 4536; b) R. Li, D. Jin, D. Pan, S. Ji, C. Xin, G. Liu, S. Fan, H. Wu, J. Li, Y. Hu, D. Wu, L. Zhang, J. Chu, *ACS Nano* **2020**, *14*, 5233.

[14] a) H.-W. Huang, M. S. Sakar, A. J. Petruska, S. Pané, B. J. Nelson, *Nat. Commun.* **2016**, *7*, 12263; b) J. H. Na, A. A. Evans, J. Bae, M. C. Chiappelli, C. D. Santangelo, R. J. Lang, T. C. Hull, R. C. Hayward, *Adv. Mater.* **2015**, *27*, 79.

[15] a) C. A. Spiegel, M. Hippler, A. Münchinger, M. Bastmeyer, C. Barner-Kowollik, M. Wegener, E. Blasco, *Adv. Funct. Mater.* **2020**, *30*, 1907615; b) C. de Marco, S. Pané, B. J. Nelson, *Sci. Robot.* **2018**, *3*, 287; c) A. S. Gladman, E. A. Matsumoto, R. G. Nuzzo, L. Mahadevan, J. A. Lewis, *Nat. Mater.* **2016**, *15*, 413; d) Z. Ding, C. Yuan, X. Peng, T. Wang, H. J. Qi, M. L. Dunn, *Sci. Adv.* **2017**, *3*, e1602890; e) Z. Wang, K. Li, Q. He, S. Cai, *Adv. Mater.* **2019**, *31*, 1806849; f) M. Falahati, P. Ahmadvand, S. Safaee, Y.-C. Chang, Z. Lyu, R. Chen, L. Li, Y. Lin, *Mater. Today* **2020**, *40*, 215; g) M. Hippler, E. Blasco, J. Qu, M. Tanaka, C. Barner-Kowollik, M. Wegener, M. Bastmeyer, *Nat. Commun.* **2019**, *10*, 232; h) D. Jin, Q. Chen, T.-Y. Huang, J. Huang, L. Zhang, H. Duan, *Mater. Today* **2020**, *32*, 19.

[16] C. Wang, L. Yang, Y. Hu, S. Rao, Y. Wang, D. Pan, S. Ji, C. Zhang, Y. Su, W. Zhu, J. Li, D. Wu, J. Chu, *ACS Nano* **2019**, *13*, 4667.

[17] L. Yang, D. Qian, C. Xin, Z. Hu, S. Ji, D. Wu, Y. Hu, J. Li, W. Huang, J. Chu, *Opt. Lett.* **2017**, *42*, 743.

[18] J. Ni, C. Wang, C. Zhang, Y. Hu, L. Yang, Z. Lao, B. Xu, J. Li, D. Wu, J. Chu, *Light: Sci. Appl.* **2017**, *6*, e17011.

[19] a) M. Rizwan, R. Yahya, A. Hassan, M. Yar, A. D. Azzahari, V. Selvanathan, F. Sonsudin, C. N. Abouloula, *Polymers* **2017**, *9*, 137; b) Y. Qiu, K. Park, *Adv. Drug Delivery Rev.* **2001**, *53*, 321.

[20] a) X. Yan, Q. Zhou, M. Vincent, Y. Deng, J. Yu, J. Xu, T. Xu, T. Tang, L. Bian, Y.-X. J. Wang, *Sci. Robot.* **2017**, *2*, eaaq1155; b) Y. Kim, E. Genevriere, P. Harker, J. Choe, M. Balicki, R. W. Regenhardt, J. E. Vranic, A. A. Dmytriw, A. B. Patel, X. Zhao, *Sci. Robot.* **2022**, *7*, eabg9907.

[21] a) M. Zarei, M. Zarei, *Small* **2018**, *14*, 1800912; b) Y. Hu, W. Liu, Y. Sun, *Adv. Funct. Mater.* **2022**, *32*, 2109181.